



ELSEVIER

Available online at [www.sciencedirect.com](http://www.sciencedirect.com)

Nuclear Instruments and Methods in Physics Research B 199 (2003) 427–435

[www.elsevier.com/locate/nimb](http://www.elsevier.com/locate/nimb)

# Phase-contrast X-ray imaging with synchrotron radiation for materials science applications

A.W. Stevenson <sup>a,\*</sup>, T.E. Gureyev <sup>a</sup>, D. Paganin <sup>a,b</sup>, S.W. Wilkins <sup>a</sup>,  
T. Weitkamp <sup>c</sup>, A. Snigirev <sup>c</sup>, C. Rau <sup>c</sup>, I. Snigireva <sup>c</sup>, H.S. Youn <sup>d</sup>, I.P. Dolbnya <sup>c</sup>,  
W. Yun <sup>e</sup>, B. Lai <sup>f</sup>, R.F. Garrett <sup>g</sup>, D.J. Cookson <sup>g</sup>, K. Hyodo <sup>h</sup>, M. Ando <sup>h</sup>

<sup>a</sup> CSIRO Manufacturing and Infrastructure Technology, Private Bag 33, Clayton South MDC, Vic. 3169, Australia

<sup>b</sup> School of Physics and Materials Engineering, P.O. Box 69M, Monash University, Vic. 3800, Australia

<sup>c</sup> European Synchrotron Radiation Facility, BP 220, 38043 Grenoble Cedex, France

<sup>d</sup> PAL, POSTECH, Pohang Institute of Science and Technology, P.O. Box 125, Pohang 790-600, South Korea

<sup>e</sup> Xradia, 4075A Sprig Drive, Concord, CA 94520-8535, USA

<sup>f</sup> Advanced Photon Source, Argonne National Laboratory, 9700 S. Cass Avenue, Argonne, IL 60439, USA

<sup>g</sup> Australian Synchrotron Research Program, c/-ANSTO, Building 16, PMB 1, Menai, NSW 2234, Australia

<sup>h</sup> Photon Factory, Institute of Materials Structure Science, High Energy Accelerator Research Organization, 1-1 Oho, Tsukuba, Ibaraki 305-0801, Japan

## Abstract

Since Röntgen's discovery of X-rays just over a century ago the vast majority of radiographs have been collected and interpreted on the basis of absorption contrast and geometrical (ray) optics. Recently the possibility of obtaining new and complementary information in X-ray images by utilizing phase-contrast effects has received considerable attention, both in the laboratory context and at synchrotron sources (where much of this activity is a consequence of the highly coherent X-ray beams which can be produced). Phase-contrast X-ray imaging is capable of providing improved information from weakly absorbing features in a sample, together with improved edge definition. Four different experimental arrangements for achieving phase contrast in the hard X-ray regime, for the purpose of non-destructive characterization of materials, will be described. Two of these, demonstrated at ESRF in France and AR in Japan, are based on parallel-beam geometry; the other two, demonstrated at PLS in Korea and APS in USA, are based on spherical-beam geometry. In each case quite different X-ray optical arrangements were used. Some image simulations will be employed to demonstrate salient features of hard X-ray phase-contrast imaging and examples of results from each of the experiments will be shown.

© 2002 Elsevier Science B.V. All rights reserved.

PACS: 41.50.+h; 42.25.-p; 07.85.Qe; 87.59.Bh

Keywords: Phase contrast; X-ray imaging; Coherence; X-ray optics

\* Corresponding author. Tel.: +61-3-9545-2917; fax: +61-3-9544-1128.

E-mail address: [andrew.stevenson@csiro.au](mailto:andrew.stevenson@csiro.au) (A.W. Stevenson).

## 1. Introduction

X-ray imaging finds application in many diverse fields including medicine, industrial inspection,

astronomy, materials science, biology, microelectronics, forensic science and security. Most of the X-ray images recorded during the last 100 years or so, starting with [1], have been collected and interpreted on the basis of absorption contrast. In terms of the complex X-ray refractive index ( $n = 1 - \delta - i\beta$ ) this means that the emphasis has been on the imaginary component  $i\beta$ , with little or no attention paid, until quite recently, to the real component  $\delta$ . It is with  $\delta$  that we are primarily concerned when dealing with X-ray phase-contrast imaging (PCI). PCI with X-rays has developed in a number of ways, utilizing both synchrotron (e.g. [2]) and laboratory (e.g. [3]) sources, including analogues of (light-) optical methods [4]. The PCI methods demonstrated in the present work are “differential” techniques (depending on the object-to-detector distance used), where the phase contrast achieved depends on a derivative (first or second) of the phase shift  $\varphi$ , and are particularly appropriate to studies which benefit from edge enhancement, e.g. examining boundaries, cracks or fibrous structure. Many examples of PCI will involve a combination of phase and absorption contrast to varying degrees and while both generally decrease with increasing X-ray energy, it is important to note that  $\delta$  varies as  $\lambda^2$  whereas  $\beta$  varies as  $\lambda^4$  ( $\lambda$  being the X-ray wavelength), in the absence of any elemental absorption edges. Hence the effects of phase contrast become progressively more dominant, relative to absorption-contrast effects, at shorter X-ray wavelengths.

A common property, which can be attributed to the various PCI methods, is the need for coherence (of the radiation), be it spatial or chromatic (or both). Many of the synchrotron-based PCI methods take advantage of the unique properties of the primary beam and also utilize specialized X-ray optical elements, to generate X-ray beams that have a high degree of both spatial and chromatic coherence. Some of these resulting X-ray beams are best described as plane waves and some as spherical waves, the latter allowing for some intrinsic magnification of features in the image plane associated with features in the object. PCI methods often rely on a relatively large object-to-detector distance to allow wave interference (Fresnel diffraction) to occur and manifest itself as

contrast in the image plane. In the present work we will be concerned only with individual X-ray PCI images, resulting from the projection of the electron-density distribution within the object along ray paths. It is however, quite feasible to employ phase contrast in the context of tomography using the methods demonstrated in the present work (e.g. [5]). Momose and co-workers, for example (e.g. [6]), have demonstrated the applicability of synchrotron radiation to PCI, including tomography, using perfect-crystal interferometers.

## 2. Image simulations

The Kirchhoff formula (e.g. [7]) has been used (with FFTs) to calculate two-dimensional X-ray intensity distributions (images) for a hypothetical object as a function of the object-to-detector distance  $R_2$  (we refer to the source-to-object distance as  $R_1$ ); see Fig. 1. The object has as its two-dimensional distribution of  $\mu t$  ( $\mu$  being the linear absorption coefficient and  $t$  the thickness), the CSIRO logo, with values of either 0 or 0.0471 (corresponding to 1 mm of carbon for 20 keV radiation). The two-dimensional distribution of  $\varphi t$  ( $\varphi$  being the phase shift per unit length) is represented by the SRMS-3 logo, with values of either 0 or  $-118.7$  (corresponding to carbon, as above). The calculations assume plane-wave illumination of the object with a 20 keV monochromatic X-ray beam and the detector is assumed to be a perfect imaging device. The object cross-sectional area (normal to the optic axis) was taken to be  $1 \text{ mm} \times 1 \text{ mm}$ . The resulting images have been truncated to  $1 \text{ mm} \times 0.5 \text{ mm}$ .

Fig. 1(a) corresponds to what is essentially a contact radiograph and as such is dominated by absorption contrast, with little contribution from phase contrast (this component would be truly zero and absorption contrast maximized for  $R_2 = 0$ ). As  $R_2$  is increased the contribution from phase contrast becomes more important and that from absorption contrast less so. In Fig. 1(b) and (c) we can see the so-called “outline” mode where the differential nature of the phase contrast is particularly evident with the edges of features associated with the  $\varphi t$  distribution being enhanced

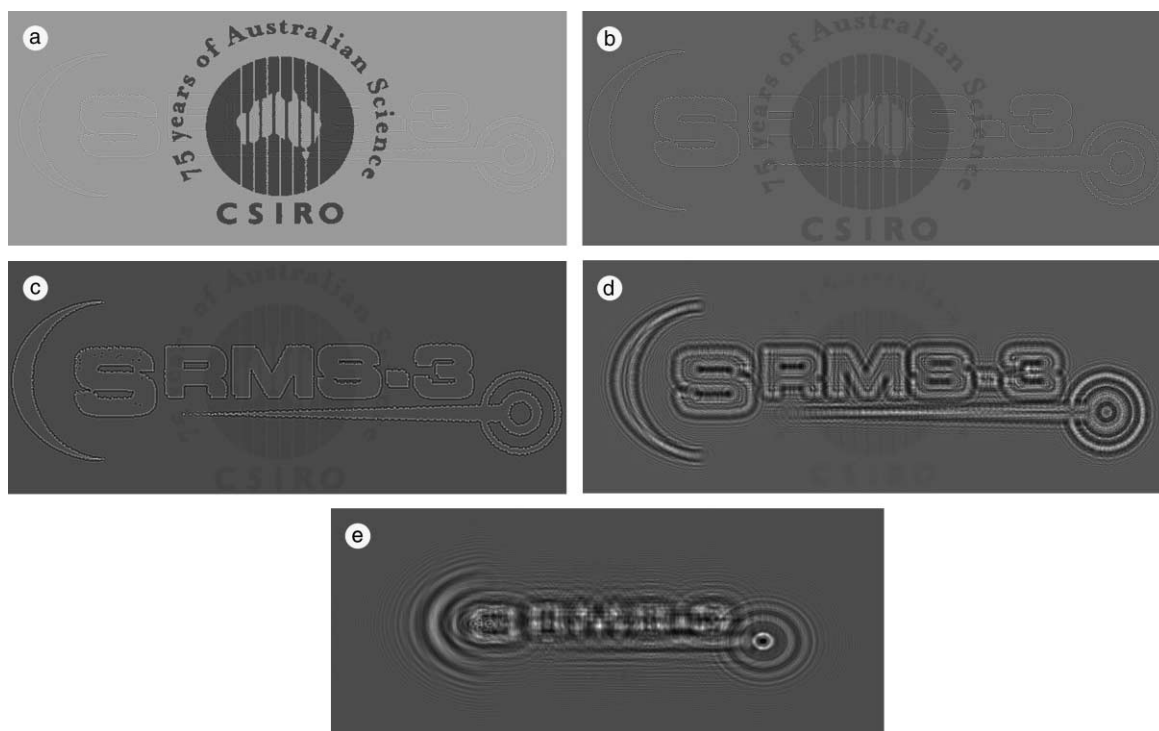


Fig. 1. Image simulations for  $R_2$  values of (a) 0.1 cm, (b) 1 cm, (c) 10 cm, (d) 100 cm and (e) 1000 cm. The respective intensity ranges are (a) [0.909, 1.04], (b) [0.544, 1.42], (c) [0.223, 2.14], (d) [0.149, 2.29] and (e) [0.00359, 2.76], where the intensity in the absence of an object is unity. The incident X-ray beam is assumed to be a monochromatic 20 keV plane wave. The image areas are  $1 \text{ mm} \times 0.5 \text{ mm}$ . The object features correspond to 1 mm thick carbon. Other details are given in the text.

by a characteristic black–white fringe. In Fig. 1(d) the multiple fringes associated with interference effects are starting to prevail and in Fig. 1(e) these interference effects dominate to the extent that the original object structure is no longer directly discernible. This is the holographic or intermediate-field regime (as opposed to the near-field regime at smaller values of  $R_2$  and the far-field regime at even larger values of  $R_2$ ) and the image can be termed an in-line hologram.

The use of sophisticated absorption- and phase-retrieval methods to extract quantitative, high-resolution, information about the object from such X-ray images as are shown in Fig. 1 is a topic of much current research. The applicability of the retrieval methods employed depends on several factors including, broadly, the imaging regime in question, and these include algorithms based on the transport-of-intensity equation (see [8]) and

iterative algorithms of the Gerchberg–Saxton type [9]. Recent examples of the application of retrieval methods to synchrotron image data are given by [10–12]. The definitions of the different imaging regimes are not well prescribed but in any event depend on  $\lambda$  and spatial frequency as well as  $R_2$  (we refer here to the plane-wave case), see also [13]. One of the challenges is to improve the retrieval methods for the holographic regime, which would enable the imaging techniques to be more usefully applied to the case of soft X-rays.

### 3. Results and discussion

#### 3.1. Examples of experiments performed at Accumulation Ring (AR), Japan

High-resolution phase-contrast X-ray images of several test objects were recorded with 33 and

38 keV X-rays using different configurations of perfect-crystal-Si monochromators and analyzers, including both Bragg and Laue geometries for the latter. The use of the 6.5 GeV TRISTAN Accumulation Ring (AR), located in Tsukuba, Japan, made it possible to employ X-ray beams of high intensity and high spatial and chromatic coherence to image weakly absorbing objects in the energy regime above 30 keV, where normal radiographs of such objects, based on absorption contrast alone, are essentially featureless. The AR was very well suited to such experiments as the brilliance was near its maximum value ( $\sim 5 \times 10^{13}$  photons/s/mm<sup>2</sup>/mrad<sup>2</sup>/0.1% bandwidth) at such photon energies (cf. a conventional bending-magnet beamline at a second-generation synchrotron source ( $\sim 1 \times 10^{11}$  photons/s/mm<sup>2</sup>/mrad<sup>2</sup>/0.1% bandwidth)), and the angular divergence in the plane of diffraction was  $\sim 5$  arcsec. The AR was operating at 6 GeV (and injected to 40 mA) during the experiments and bending-magnet beamline NE5A was used. Three different experimental configurations were used for the PCI experiments: (i) an asymmetric (negative asymmetry) Bragg-geometry 311 single-reflection monochromator used with a symmetric Bragg-geometry 311 single-reflection analyzer; (ii) the previous monochromator with a symmetric 311 Laue-geometry analyzer; (iii) a 311 double-reflection (both negative asymmetry Bragg-geometry) monochromator with the previous analyzer. The monochromator was placed approximately 15 m from the source. In those cases where a Laue-geometry analyzer was used both the reflected and transmitted beams can be used for imaging. High-resolution X-ray film was used to record the images. Further details of the experiments, including details of the monochromator and analyzer designs and performance, considerations of the suppression of harmonic contamination, and so on, will be presented elsewhere.

Fig. 2 shows a phase-contrast image of an aerospace material comprising two thin sheets of aluminium separated by an epoxy film adhesive. Voids in the adhesive with sizes below 100  $\mu\text{m}$  are clearly visible, with the typical void size being of order 200  $\mu\text{m}$ . This image was recorded at 33 keV with the third geometry mentioned above and with

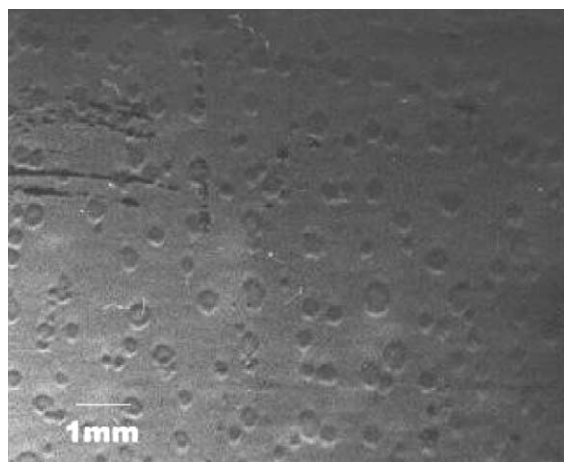


Fig. 2. X-ray phase-contrast image of an aerospace material comprising two thin sheets of aluminium separated by an epoxy film adhesive recorded at AR, Japan. Voids in the adhesive with sizes below 100  $\mu\text{m}$  are clearly visible, with the typical void size being of order 200  $\mu\text{m}$ .

the film intercepting the transmitted beam from the analyzer crystal (oriented to the peak of the rocking curve). Fig. 3 shows a phase-contrast image of a section of a thin succulent leaf, including the main stem. This image was recorded at 33 keV with the second geometry mentioned above and with the film intercepting the transmitted beam. In both cases the absorption contrast at such X-ray energies is insignificant, whereas the phase-contrast effects are clearly evident.

### 3.2. Examples of experiments performed at Advanced Photon Source (APS), USA

SRI-CAT beamline 2-ID-D at the 7 GeV Advanced Photon Source (APS) in USA was used to perform PCI experiments in spherical-wave geometry by using a Fresnel zone plate (focal length 5 cm at 8 keV). A 10  $\mu\text{m}$  pin-hole was placed between the zone plate and the object as an ordering aperture. The field-of-view on the object was approximately 50  $\mu\text{m}$ ,  $R_1 = 5$  cm and  $R_2 = 50$  cm. A liquid-nitrogen cooled Photometrics CCD equipped with a CdWO<sub>4</sub> scintillator crystal and lens in front and having 20  $\mu\text{m}$  pixels was used to record the images. A He-filled tube was used be-

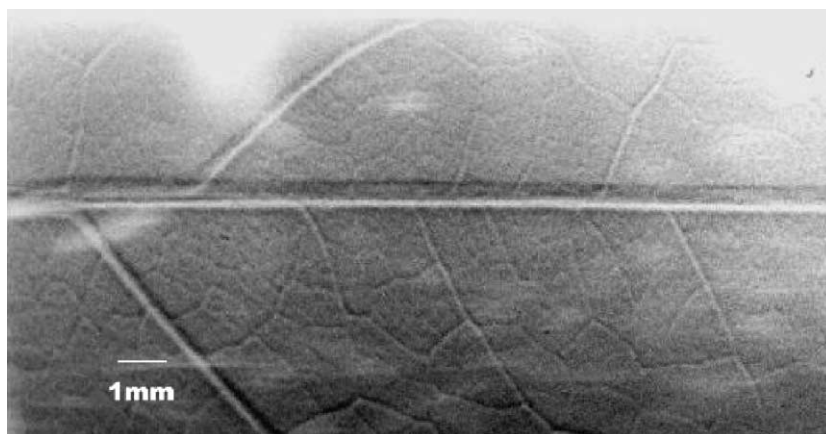


Fig. 3. X-ray phase-contrast image of a section of a thin succulent leaf, including the main stem recorded at AR, Japan.

tween the main window at the hutch entrance and the zone plate. Flat-field images (no object), but not dark-current images, were also recorded throughout the experiments although these have not been used in the present work. Further details of the experiments, including details of the X-ray optical elements used further upstream, will be presented elsewhere.

Fig. 4 shows a phase-contrast image of a thin plastic film edge. Multiple fringes are clearly visible and it is apparent that there are contributions due to imperfections of the film edge. Some artifacts of the imaging system are also visible and these can be corrected to some extent by dividing by the corresponding flat-field images. Fig. 5 shows a phase-contrast image for a 100  $\mu\text{m}$  thick cross-section of hardwood.

### 3.3. Examples of experiments performed at Pohang Light Source (PLS), Korea

The fluorescence radiation from a thin metal film deposited on a thin Si substrate, or a thin metal foil was used to record (quasi-monochromatic) phase-contrast images in an essentially window-less configuration, thereby avoiding the artefacts associated with, for example, inhomogeneous Be windows. The dependence of image contrast on spatial coherence of the X-ray beam could be investigated by varying the effective

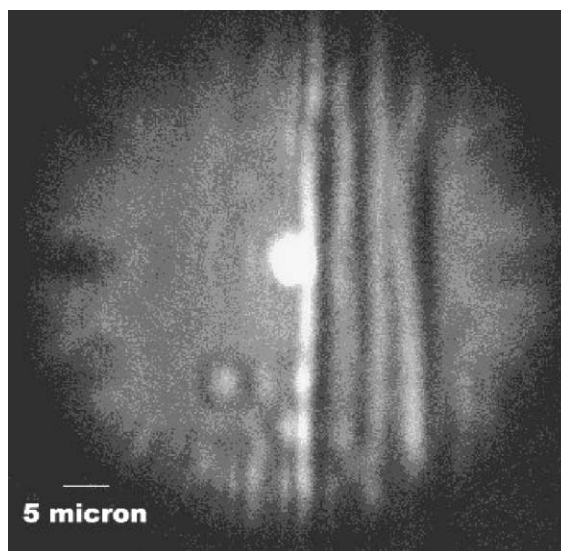


Fig. 4. X-ray phase-contrast image of a thin plastic film edge recorded with a CCD at APS, USA. No flat-field correction has been applied.

source size. A tapered glass capillary (focal length 4 cm) was employed to concentrate the synchrotron beam on to a small spot on the metal-film or metal-foil target. The experiments were performed at beamline 1B3 of the Pohang Light Source (PLS), operating at 2 GeV, in Korea. The tapered glass capillary was mounted with remotely

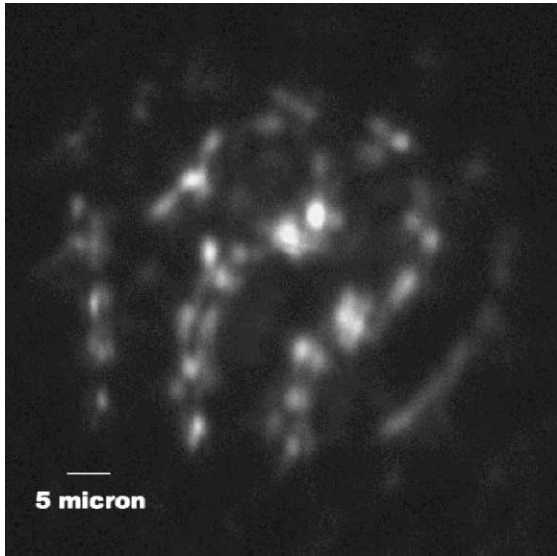


Fig. 5. X-ray phase-contrast image of a 100  $\mu\text{m}$  thick cross-section of hardwood recorded with a CCD at APS, USA. No flat-field correction has been applied.

controlled  $X$ – $Y$  stages at each end and was aligned with the aid of a ZnS screen. The “secondary beamline” was set up at approximately right an-

gles to the primary synchrotron beam to avoid unwanted scatter as much as possible and to take advantage of the plane-polarization of the synchrotron radiation in the horizontal plane. Considerable effort was spent on arranging shielding so that unwanted scatter did not reach the X-ray film and, with a long beam path to the film (of order 1 m), a He-filled tube was used. This tube was sealed with thin, high-quality, polyimide windows to avoid degrading the image quality. A Si(Li) detector was used to check the fluorescence spectrum.  $R_1$  and  $R_2$  were typically of order 20 and 120 cm, respectively (but were varied during the experiments) and we are dealing with spherical-wave geometry. The experimental arrangement used also meant that the effective horizontal source size was foreshortened (as seen by the object) and could, in some cases, be extremely small, e.g. when using a 300 nm Cu layer deposited on a 50  $\mu\text{m}$  Si wafer as the target. In the case of targets of thin metal films on substrates the fluorescence could be altered by having the substrate on the upstream or downstream side. Further details of the experiments, including details of the X-ray optical elements used further upstream, will be presented elsewhere.

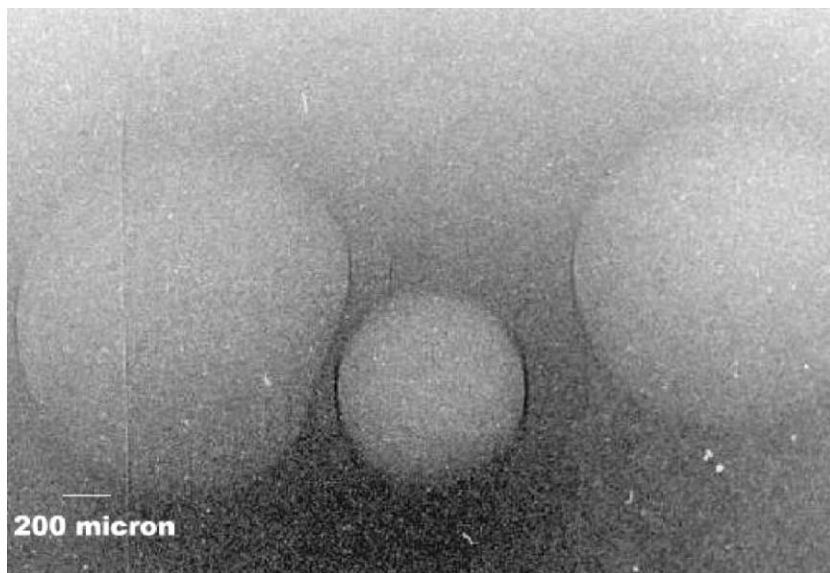


Fig. 6. X-ray phase-contrast image of a phantom comprising air bubbles and thin glass fibres in a thin polymer matrix recorded with experimental magnification ( $M = (R_1 + R_2)/R_1$ ) of approximately 4 ( $R_1 = 37$  cm and  $R_2 = 118$  cm) at PLS, Korea.

Fig. 6 shows a phase-contrast image of a phantom comprising air bubbles and thin glass fibres in a thin polymer matrix recorded with a 50  $\mu\text{m}$  Ni foil as the target and an experimental magnification ( $M = (R_1 + R_2)/R_1$ ) of approximately 4. Particularly noteworthy in this image is the effect of the foreshortening of the effective source size horizontally, the edges of the bubbles running near-vertically being very sharp and a glass fibre which is running near-vertically showing up very clearly on the left-hand-side. Fig. 7 shows a phase-contrast image of a specially prepared 75  $\mu\text{m}$  thick polyimide film with a (nominally) 40  $\mu\text{m}$  period structure (20  $\mu\text{m}$  deep), recorded with the same target and  $M$  approximately 15.

#### 3.4. Examples of experiments performed at European Synchrotron Radiation Facility (ESRF), France

Undulator beamline ID 22 at the 6 GeV European Synchrotron Radiation Facility (ESRF), France was used to collect phase-contrast images

using a parallel-beam geometry. A Pt-coated Si mirror and a fixed-exit double-reflection Si 111 monochromator were used to condition the primary X-ray beam. The objects to be imaged were located approximately 60m from the source. A FreLoN-2000 CCD camera developed at the ESRF was used with a lutetium aluminium garnet scintillator screen and lens in front, to record the X-ray images. The effective pixel size was 0.33  $\mu\text{m}$ . Flat-field and dark-current images were collected throughout the experiments. Further details of the experiments are provided in [11] and will also be presented elsewhere.

Fig. 8 shows a phase-contrast image recorded at 20 keV with  $R_2 = 20$  cm for an Al sample containing graphite fibres. Phase-contrast effects are quite pronounced at the edges of individual fibres. Fig. 9 shows a phase-contrast image recorded under the same conditions for a section of a feather encompassing the main quill. Both flat-field and dark-current corrections have been performed for Fig. 9, but only flat-field correction for Fig. 8.

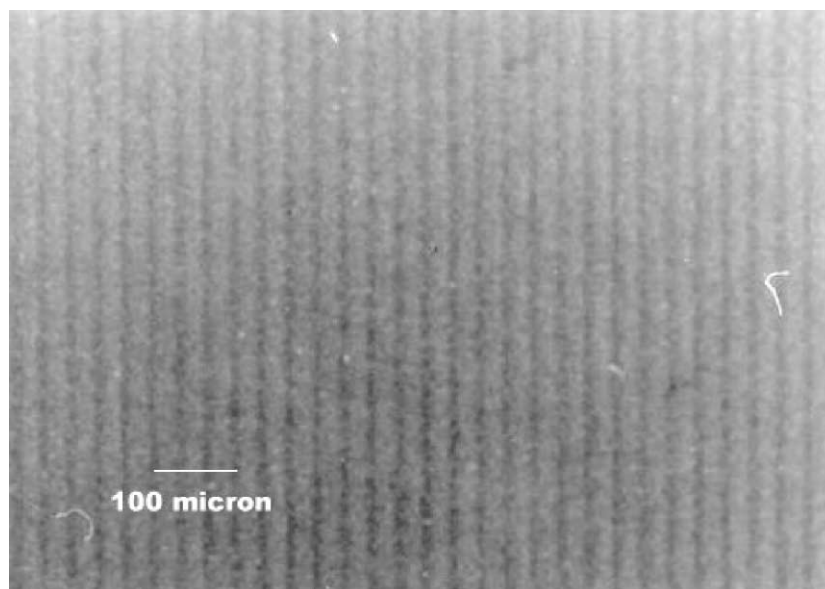


Fig. 7. X-ray phase-contrast image of a 75  $\mu\text{m}$  thick polyimide film with a (nominally) 40  $\mu\text{m}$  period structure (20  $\mu\text{m}$  deep) recorded with  $M$  approximately 15 ( $R_1 = 10.5$  cm and  $R_2 = 145.5$  cm) at PLS, Korea.

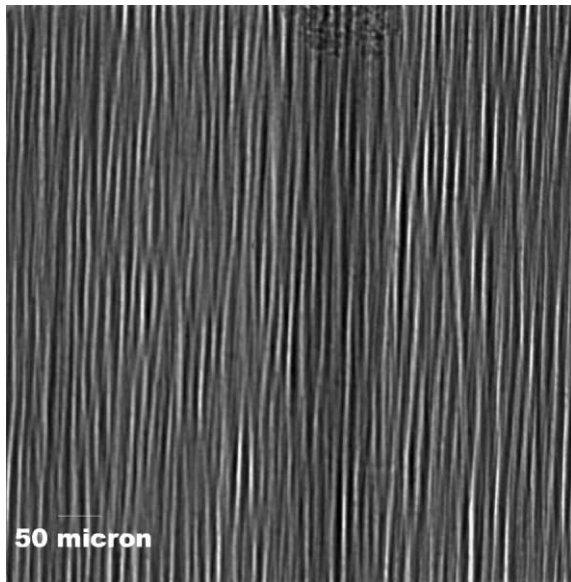


Fig. 8. X-ray phase-contrast image of an Al/graphite-fibre sample recorded at 20 keV and  $R_2 = 20$  cm at ESRF, France. Flat-field correction has been applied.

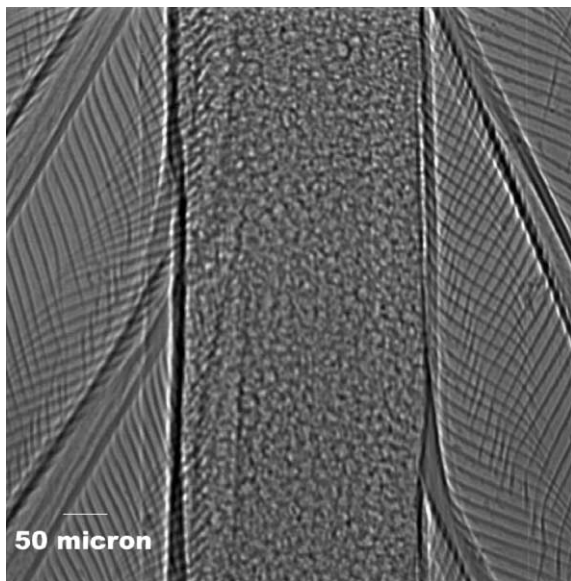


Fig. 9. X-ray phase-contrast image of a feather recorded at 20 keV and  $R_2 = 20$  cm at ESRF, France. Flat-field and dark-current corrections have been applied.

#### 4. Conclusions

We have demonstrated some of the benefits of hard X-ray PCI, implemented in various ways (including both plane-wave and spherical-wave geometries) using synchrotron radiation, by way of simple examples. Image simulations have also been used to point out some of the important features of this contrast mechanism.

#### Acknowledgements

The Australian Synchrotron Research Program and the “Access to Major Research Facilities Program” managed by the Australian Nuclear Science and Technology Organization are acknowledged for supporting this work and funding the overseas visits of some of the Australian co-authors to conduct the experiments. Use of the APS was supported by the US Department of Energy, Basic Energy Sciences, Office of Science, under contract no. W-31-109-Eng-38. Some of the Australian co-authors also wish to acknowledge financial support from X-ray Technologies Pty. Ltd. toward the ESRF component of the work described. Drs. D. Arnott, S. Burke, R. Evans, E. Harvey and A. Wilson are thanked for providing samples and Drs. D. Balaic and D. Gao for providing certain X-ray optical elements.

#### References

- [1] W.C. Röntgen, Sitzungber. Phys.-Med. Gesellschaft Würzburg, (1895) 132 (Translated into English in Nature 53 (1896) 274).
- [2] A. Snigireva, I. Snigireva, V. Kohn, S. Kuznetsov, I. Schelokov, Rev. Sci. Instrum. 66 (1995) 5486.
- [3] S.W. Wilkins, T.E. Gureyev, D. Gao, A. Pogany, A.W. Stevenson, Nature 384 (1996) 335.
- [4] F. Zernike, Z. Tech. Phys. 16 (1935) 454.
- [5] P. Cloetens, M. Pateyron-Salomé, J.Y. Buffière, G. Peix, J. Baruchel, F. Peyrin, M. Schlenker, J. Appl. Phys. 81 (1997) 5878.
- [6] A. Momose, T. Takeda, Y. Itai, Rev. Sci. Instrum. 66 (1995) 1434.
- [7] J.M. Cowley, Diffraction Physics, North-Holland, Amsterdam, 1975.
- [8] M.R. Teague, J. Opt. Soc. Am. 73 (1983) 1434.
- [9] R.W. Gerchberg, W.O. Saxton, Optik 35 (1972) 237.

- [10] T.E. Gureyev, C. Raven, A. Snigirev, I. Snigireva, S.W. Wilkins, J. Phys. D: Appl. Phys. 32 (1999) 563.
- [11] T.E. Gureyev, A.W. Stevenson, D.M. Paganin, T. Weitkamp, A. Snigirev, I. Snigireva, S.W. Wilkins, J. Synch. Rad. 9 (2002) 148.
- [12] B.E. Allman, P.J. McMahon, J.B. Tiller, K.A. Nugent, D. Paganin, A. Barty, I. McNulty, S.P. Frigo, Y. Wang, C.C. Retsch, J. Opt. Soc. Am. A 17 (2000) 1732.
- [13] A. Pogany, D. Gao, S.W. Wilkins, Rev. Sci. Instrum. 68 (1997) 2774.